

(compare Figs. 2 and 3). The first is centered on the point of release and the second on the position of the nest location. Because both contribute to the entire data distribution, the median value lies around roughly half the distance between the releasing point and the nest position. The IT and BF groups do not show such a distinct second search phase; thus, the data are distributed around the point of release.

Our experiments show that the exclusive use of OF cues is sufficient for the ants to measure travel distances. Furthermore, active locomotion is not a prerequisite for distance estimation or path integration, provided that the transport happens in a naturally occurring behavior (17). There is ample evidence that the stride integrator can function without visual input. Ants walking in complete darkness (18), or with the ventral halves of their eyes covered (8, 9), are still able to gauge homing distance correctly. However, our results show that two separate and independent systems of distance measurement exist and operate redundantly.

REFERENCES AND NOTES

- M. Müller, R. Wehner, *Proc. Natl. Acad. Sci. U.S.A.* **85**, 5287–5290 (1988).
- R. Wehner, M. V. Srinivasan, in *The Neurobiology of Spatial Behaviour*, K. J. Jeffrey, Ed. (Oxford Univ. Press, 2003), chap. 1, pp. 9–30.
- M. Wittlinger, R. Wehner, H. Wolf, *Science* **312**, 1965–1967 (2006).
- M. Wittlinger, R. Wehner, H. Wolf, *J. Exp. Biol.* **210**, 198–207 (2007).
- H. E. Esch, J. E. Burns, *Naturwissenschaften* **82**, 38–40 (1995).
- M. V. Srinivasan, S. Zhang, M. Altwein, J. Tautz, *Science* **287**, 851–853 (2000).
- A. Ugolini, *Anim. Behav.* **35**, 590–595 (1987).
- B. Ronacher, R. Wehner, *J. Comp. Physiol. A* **177**, 21–27 (1995).
- M. Wittlinger, H. Wolf, *J. Physiol. Paris* **107**, 130–136 (2013).
- M. Möglich, B. Hölldobler, *Psyche* **81**, 219–236 (1974).
- P. Duelli, *Rev. Suisse Zool.* **83**, 413–418 (1976).
- P. Duelli, *Rev. Suisse Zool.* **80**, 712–719 (1973).
- A. Dabhi, J. Retana, A. Lenoir, X. Cerdà, *J. Ethol.* **26**, 119–126 (2008).
- Materials and methods are available as supplementary materials on Science Online.
- S. E. Pfeffer, M. Wittlinger, *J. Exp. Biol.* **219**, 2119–2126 (2016).
- F. Leubhardt, B. Ronacher, *J. Comp. Physiol. A* **201**, 599–608 (2015).
- T. Seidl, M. Knaden, R. Wehner, *J. Comp. Physiol. A* **192**, 1125–1131 (2006).
- M. Thiélin-Bescond, G. Beugnon, *Naturwissenschaften* **92**, 193–197 (2005).

ACKNOWLEDGMENTS

We thank H. Wolf for help during the initial experiments, discussions, and support; K. J. Kaiser and V. L. Wahl for help collecting data in the field; O. Stroh for measuring the head angles, and U. Seifert for editing the text. The University of Ulm provided financial support and infrastructure. M.W. developed the initial idea and concept. M.W. and S.E.P. planned and carried out the experiments, analyzed the data, and wrote the manuscript. Data are available on Dryad (doi:10.5061/dryad.8h3n).

SUPPLEMENTARY MATERIALS

www.sciencemag.org/content/353/6304/1155/suppl/DC1
Materials and Methods
Supplementary Text
Figs. S1 and S2
References (19–21)
Movie S1

28 April 2016; accepted 17 August 2016
10.1126/science.aaf9754

CELL MIGRATION

Collective cell durotaxis emerges from long-range intercellular force transmission

Raimon Sunyer,¹ Vito Conte,¹ Jorge Escribano,² Alberto Elosegui-Artola,¹ Anna Labernadie,¹ Léo Valon,¹ Daniel Navajas,^{1,3,4} José Manuel García-Aznar,² José J. Muñoz,⁵ Pere Roca-Cusachs,^{1,3*} Xavier Trepát^{1,3,6,7*}

The ability of cells to follow gradients of extracellular matrix stiffness—durotaxis—has been implicated in development, fibrosis, and cancer. Here, we found multicellular clusters that exhibited durotaxis even if isolated constituent cells did not. This emergent mode of directed collective cell migration applied to a variety of epithelial cell types, required the action of myosin motors, and originated from supracellular transmission of contractile physical forces. To explain the observed phenomenology, we developed a generalized clutch model in which local stick-slip dynamics of cell-matrix adhesions was integrated to the tissue level through cell-cell junctions. Collective durotaxis is far more efficient than single-cell durotaxis; it thus emerges as a robust mechanism to direct cell migration during development, wound healing, and collective cancer cell invasion.

The ability of living cells to migrate following environmental gradients underlies a broad range of phenomena in development, homeostasis, and disease (1, 2). The best-understood mode of directed cell migration is chemotaxis, the well-established ability of cells to follow gradients of soluble chemical cues (1). Some cell types are also able to follow gradients in the stiffness of their extracellular matrix (ECM), a process known as durotaxis (3–10). Durotaxis has been implicated in development (11), fibrosis (12), and cancer (13), but its underlying mechanisms remain unclear.

Most of our understanding of directed cell migration has been obtained in single isolated cells. However, fundamental processes during development, wound healing, tissue regeneration, and some forms of cancer cell invasion are driven by directed migration of cell groups (14–16). Cell-cell interactions within these groups provide cooperative mechanisms of cell guidance that are altogether inaccessible to single cells (14–20). Here, we investigated whether cell groups undergo collective durotaxis and the cooperative nature of underlying mechanisms.

Using stencils of magnetic polydimethylsiloxane (PDMS), we micropatterned rectangular clusters (500 μm in width) of human mammary epithelial cells (MCF-10A) on fibronectin-coated polyacrylamide gel substrates exhibiting either uniform stiffness or a stiffness gradient (56.6 ± 2.1 kPa/mm) (fig. S1) (21, 22). Upon removal of the PDMS stencil, clusters migrating on uniform gels displayed symmetric expansion (Fig. 1, A, C, E, and G; fig. S2A; and movie S1), whereas clusters migrating on stiffness gradients displayed a pronounced asymmetry characterized by faster, more persistent expansion toward the stiff edge (Fig. 1, B, D, F, and H; fig. S2, B to F; and movie S1). This

result was also observed in clusters of Madin-Darby canine kidney epithelial cells (MDCK) and three-dimensional spheroids of human epidermoid carcinoma cells (A431) (fig. S3).

Asymmetric expansion is not attributable to cell proliferation, because it was unaffected by inhibition of cell division and because the number of divisions in the cluster was independent of substrate stiffness (fig. S4). Importantly, it is not attributable to additive contribution of single-cell durotaxis either, because single MCF-10A cells did not durotax in isolation (Fig. 2, A to C and E, and movie S2). Taken together, these data establish an unanticipated mode of collective durotaxis driven by an emergent property of the cell cluster.

Even if single MCF-10A cells did not durotax in isolation, they exhibited faster randomly oriented velocity on stiffer gels (Fig. 2D) (13). In a close-packed system, this feature could explain collective durotaxis because volume exclusion would force cells to move persistently away from the cluster at a higher speed on the stiffer edge. To test the contribution of this mechanism, we perturbed cell-cell junctions independently of close packing by knocking down α -catenin using small interfering RNA (siRNA). Like control cells,

¹Institute for Bioengineering of Catalonia, 08028 Barcelona, Spain. ²Aragon Institute of Engineering Research (I3A), University of Zaragoza, 50018 Zaragoza, Spain. ³University of Barcelona, 08028 Barcelona, Spain. ⁴Centro de Investigación Biomédica en Red en Enfermedades Respiratorias, 28029 Madrid, Spain. ⁵Laboratory of Numerical Analysis (LaCaN), Polytechnic University of Catalonia (UPC-BarcelonaTech), 08036 Barcelona, Spain. ⁶Institució Catalana de Recerca i Estudis Avançats (ICREA), Barcelona, Spain. ⁷Centro de Investigación Biomédica en Red en Bioingeniería, Biomateriales y Nanomedicina, 28029 Madrid, Spain.

*Corresponding author. Email: roca-cusachs@ub.edu (P.R.-C.); xtrepát@ibecbarcelona.eu (X.T.)

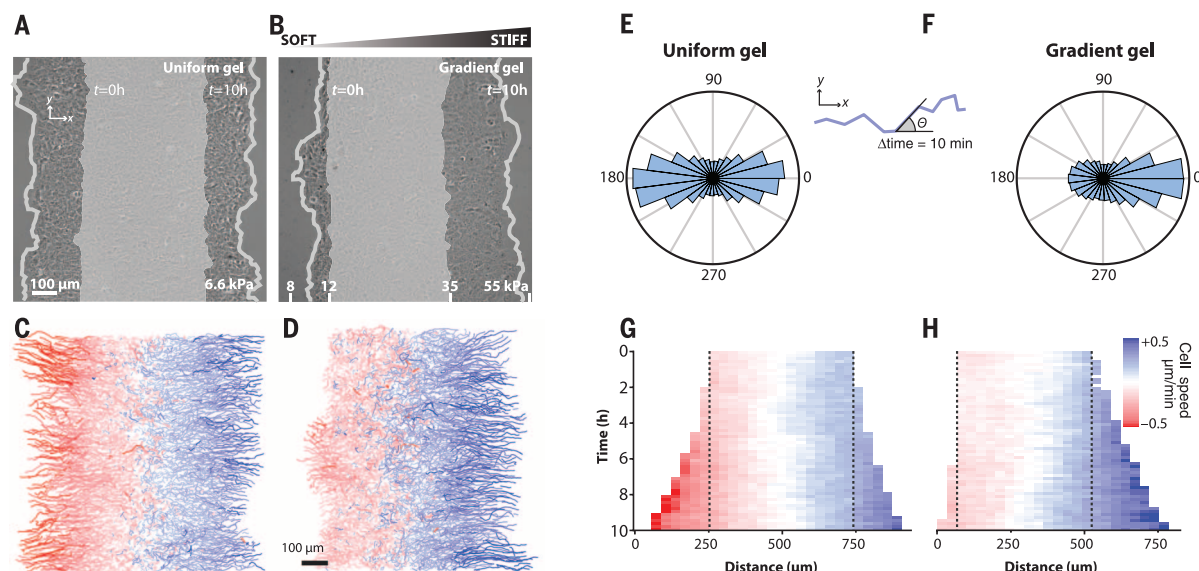
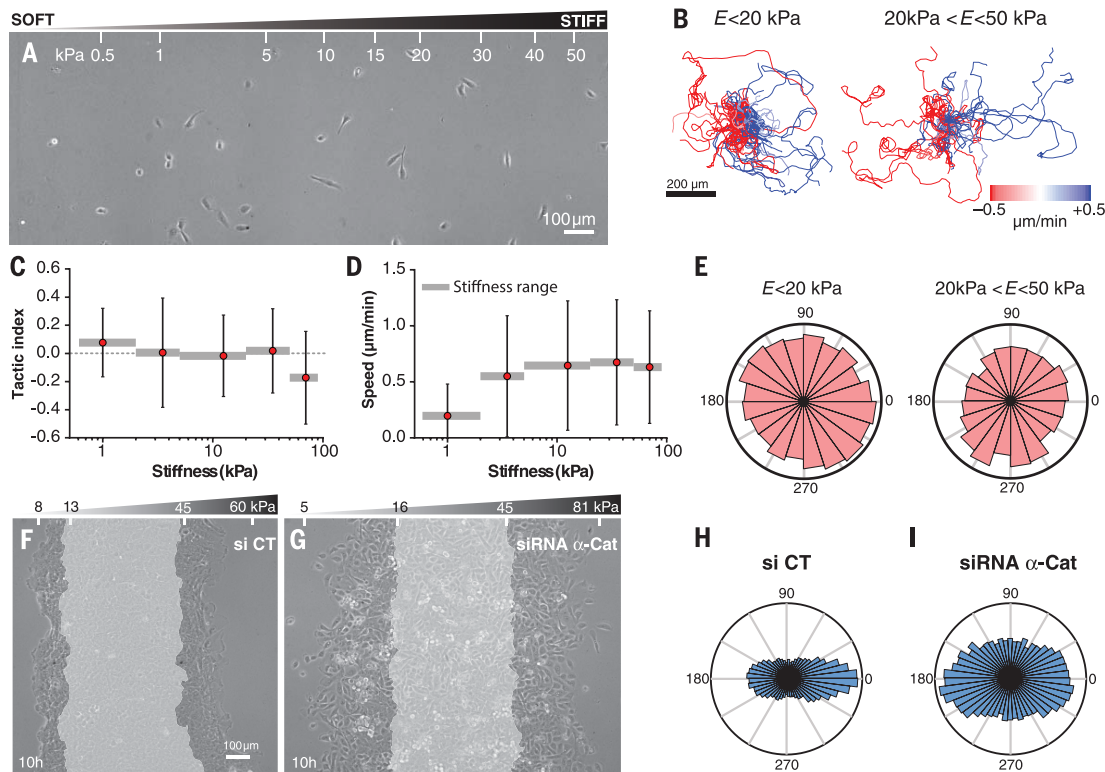


Fig. 1. Cell clusters display durotaxis. (A) A representative cell cluster expanding on a soft uniform gel of 6.6 kPa. The gray transparent area indicates initial cluster position ($t = 0$ hours), and the phase-contrast image shows the cluster at 10 hours. Gray lines indicate cluster edges at 10 hours. (B) Example of a cell cluster expanding on a gradient gel. Gel stiffness increases toward the right of the panel. Numbers at the bottom indicate Young's modulus values measured with atomic force microscopy (AFM). (C and D) Individual cell trajectories corresponding to the experiments displayed in (A) and (B),

respectively. Color coding indicates mean cell speed for every track. (E and F) Distribution of the angle θ between the instantaneous velocity vector and the x axis (see inset) for the experiments displayed in (A) and (B), respectively. (G and H) x - t Kymographs of cell speed corresponding to the experiments displayed in (A) and (B), respectively. Dashed lines indicate initial cluster position. Kymographs were computed by averaging the speed of individual trajectories in the x direction over the y coordinate for every time point (methods).

Fig. 2. Collective durotaxis is an emergent phenomenon.

(A) Phase-contrast image of MCF-10A cells seeded at low density on a gradient gel. Gel stiffness increases toward the right of the image. Numbers at the top of the panel indicate Young's modulus values measured with AFM. (B) Trajectories of individual cells located in different regions of the gradient gel. For the two regions of the gel, trajectories are plotted with the same origin. Color coding indicates mean cell speed. (C and D) Mean tactic index (C) and mean speed (D) of single cells located in different regions of the gradient gel (see Methods). Horizontal gray bars indicate the stiffness range of each bin. Error bars are SD of $n = 24$ to 63 cells. (E) Angular distributions of cell trajectories in different regions of the gradient gels. (F and G) Example of a control cluster (F) and a cluster depleted of α -catenin (G) expanding on a gradient gel. Gray area indicates initial cluster position ($t = 0$ hours), and phase-contrast image shows the cluster at 10 hours. Western blot analysis showed that α -catenin levels on the day of the experiment were $57 \pm 13\%$ of those observed in control cells. (H and I) Angular distributions of cell trajectories for experiments shown in (F) and (G), respectively.



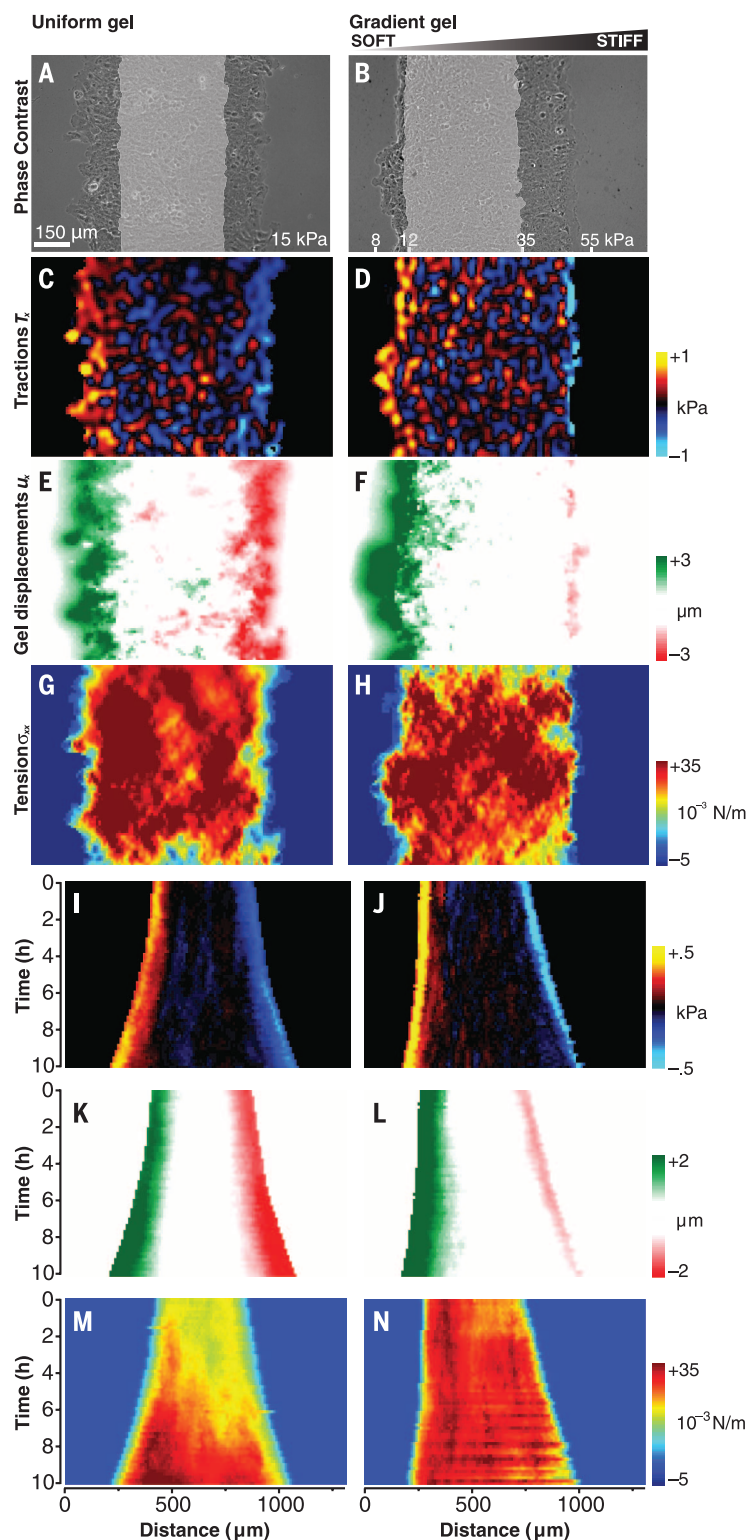


Fig. 3. Traction force microscopy on gradient gels shows long-range intercellular force transmission within the clusters. (A and B) Phase-contrast images of clusters migrating on a uniform gel (A) and on a gradient gel (B). (C and D) Maps of the traction component T_x . (E and F) Maps of the substrate displacement component u_x . (G and H) Maps of the intercellular tension component σ_{xx} for the clusters depicted in (A) and (B). (I and J) Kymographs of the traction component T_x for a uniform gel (I) and for a gradient gel (J). (K and L) Kymographs of the substrate displacement component u_x . (M and N) Kymographs of intercellular tension component σ_{xx} . See fig. S14 for all other components of tractions, intercellular stress tensor, and substrate displacements.

isolated cells depleted of α -catenin migrated faster on stiffer regions but did not durotax (fig. S5, A to D, and movie S3). Unlike control clusters, however, close-packed clusters depleted of α -catenin expanded nearly symmetrically (Fig. 2, F to I; fig. S5, E to M; and movie S4), thereby indicating that cell-cell adhesions are required for collective cell durotaxis. These findings rule out mechanisms solely based on local stiffness sensing and point to a long-range mechanism involving cell-cell adhesion.

We next studied whether this long-range mechanism involves transmission of physical forces across the cluster. To this end, we implemented a generalized traction force microscopy algorithm to map forces exerted by cells on substrates with arbitrary stiffness profiles (supplementary text 1). Clusters migrating on uniform gels (Fig. 3, A and C, and movie S5) and on gradient gels (Fig. 3, B and D, and movie S6) exhibited similar traction force maps. The highest tractions were localized at the edges and pointed toward the midline of the cluster, whereas relatively lower tractions in the bulk showed no particular orientation. To average out fluctuations and retain systematic traction patterns, we computed x - t kymographs of traction component T_x (Fig. 3, I to J). Kymographs on uniform and gradient gels revealed two traction layers of similar magnitude and opposite sign at both edges of the clusters and negligible average tractions in the bulk. Interestingly, soft edges had cell-substrate forces similar to those of stiff edges but smaller and denser cell-matrix adhesions, consistent with previous findings that force levels are not necessarily linked to a specific adhesion size (fig. S6, A and B) (23). Unlike traction forces, substrate displacements on gradient gels were nearly one order of magnitude higher on the soft edge than on the stiff one (Fig. 3, E, F, K, and L, and movies S5 and S6).

To compute force transmission within the monolayer, we used monolayer stress microscopy and focused on the normal component of the stress tensor in the direction of expansion σ_{xx} (24, 25), which we hereafter refer to as intercellular tension (Fig. 3, G and H, and movies S5 and S6). Kymographs showed that intercellular tension increased up to a plateau within the first few cells at the monolayer edges and remained roughly constant in the monolayer bulk thereafter (Fig. 3, M and N).

Our force measurements establish that the monolayer expands by generating contractile traction forces of equal magnitude at both edges and that these forces are transmitted across the cluster. To explore how this physical scenario might lead to collective durotaxis, we developed a model that integrates clutchlike cell-ECM dynamics at focal adhesions (23, 26–28), long-range force transmission through cell-cell junctions, and actin polymerization at monolayer edges (Fig. 4, A and B, and supplementary text 2). For a monolayer attached to a substrate of uniform stiffness, the model predicts symmetric expansion; actin polymerization exceeds acto-myosin contraction to the same extent on both edges.

By contrast, on stiffness gradients, the substrate deforms and opposes polymerization more on the soft edge, tilting monolayer expansion toward the stiff one (Fig. 4B).

We next used the model to produce testable predictions. First, the model predicts that durotaxis should decrease upon reducing the difference in substrate deformation between the soft and stiff side (Fig. 4C). We confirmed this prediction by reducing the slope of the stiffness gradient (Fig. 4D), seeding clusters on progressively stiffer regions of the gradient gels (Fig. 4D), reducing cluster size (fig. S7), inhibiting myosin contractility with blebbistatin (Fig. 4, E to H; fig. S8; and movie S7), and reducing cell adhesion by decreasing fibronectin coating (fig. S9). Notably, clusters placed on the softest region of the gradient, where the model predicts highest durotaxis, exhibited directed migration toward the stiff edge as a single unit rather than asymmetric expansion (fig. S10 and movie S8). Second, impairing long-range force transmission should abrogate durotaxis. This prediction was confirmed

by knocking down α -catenin (Fig. 2, F to I; fig. S11; and movie S9) and by laser-ablating clusters in the direction parallel to the midline (Fig. 4, I to L; fig. S12; and movie S10), which drastically reduced both intercellular force transmission and durotaxis. Third, the clutch mechanism implies that actin retrograde flow should be faster on the soft edge and that the differences in the speeds of actin flow and monolayer expansion between edges should be of the same order. This was indeed the case (fig. S6, C and D). Finally, the model predicts that in response to an extremely steep gradient, even single cells should generate sufficiently large differences in substrate deformation between their leading and trailing edges to enable durotaxis (10). As predicted, single MCF-10A cells exhibited weak but significant durotaxis in response to a step gradient (433.6 ± 43.6 kPa/mm) (fig. S13). Given the close agreement between model predictions and experiments, we conclude that local stiffness sensing at the cluster edges and long-range force transmission through intercellular junctions are sufficient

to explain the phenomenology of collective cell durotaxis.

Recent experimental and theoretical research has emphasized that some collective systems are more effective at responding to environmental gradients than their isolated constituents (19, 20, 29). This emergent phenomenon, often alluded to as “collective intelligence,” has been observed in cell clusters during chemotaxis (19, 20), fish schools during phototaxis (29), and human groups during online gaming (30). In the context of these phenomena, collective durotaxis is unique in that the very same machinery that senses the attractant—i.e., the actomyosin cytoskeleton—is responsible for propulsion toward it. As such, collective durotaxis might be the most rudimentary, and perhaps most primitive, mechanism by which a collective living system responds to a gradient. Rudimentary or not, collective durotaxis is robust, is general, and dramatically boosts single-cell responses, providing a new mechanism to organize directed cell migration during development, wound healing, and collective cancer cell invasion.

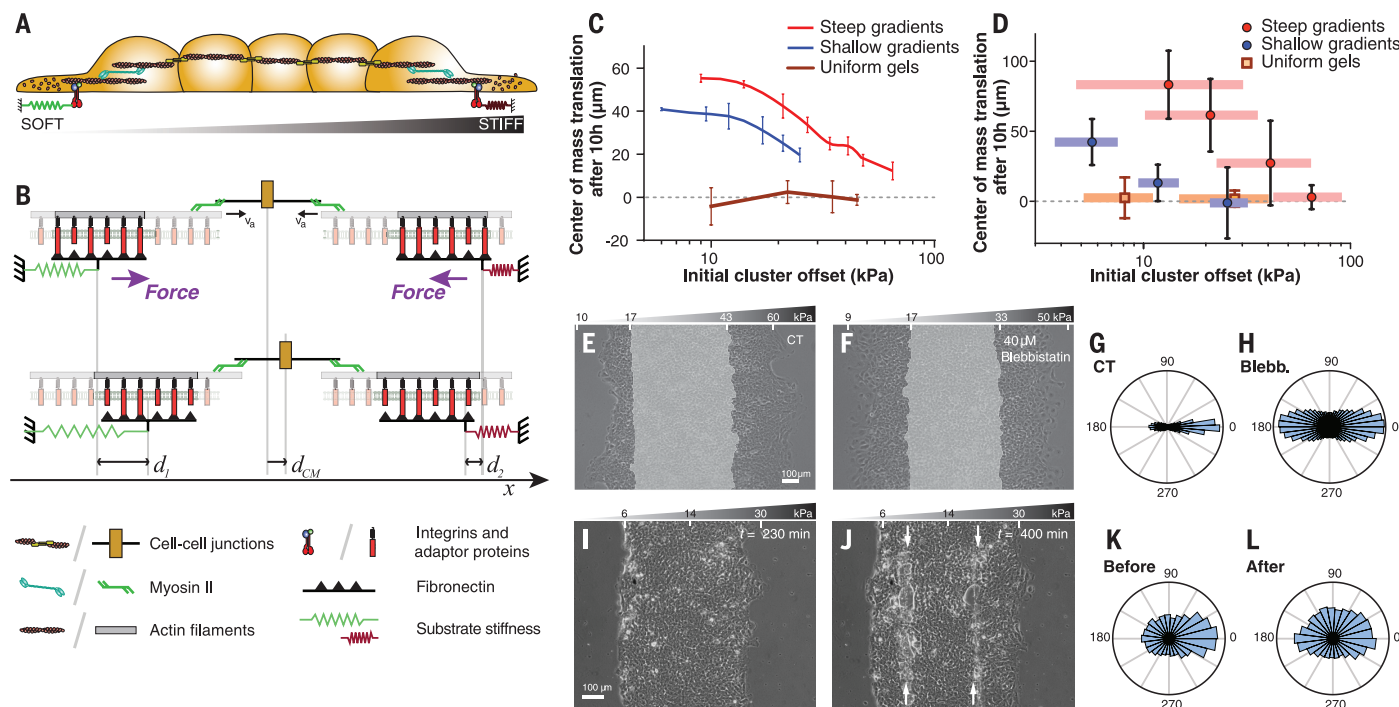


Fig. 4. A generalized clutch model predicts collective durotaxis. (A) The expanding cell monolayer is modeled as a one-dimensional contractile continuum that exerts forces on its underlying deformable substrate through discrete focal adhesions and viscous friction. (B) (Top) Each focal adhesion is modeled as a clutch. Actomyosin-driven contraction of the monolayer causes substrate deformation and actin retrograde flow according to the binding/unbinding dynamics of focal adhesion proteins under force. Substrate deformation is represented as a deformed discrete spring for simplicity, but the model is continuum (see supplementary text 2). (Bottom) To maintain force balance across the monolayer after each myosin-driven contraction step, the substrate is pulled by a larger amount on the soft side (d_1) than on the stiff side (d_2), thereby tilting overall expansion toward the stiff side ($d_{CM} = d_1 - d_2$). (C) Model predictions. Durotaxis (quantified by the cluster center of mass translation after 10 hours) represented as a function of the initial stiffness of the center of the

cluster (i.e., stiffness offset). Error bars are SD of $n = 5$ simulations. (D) Experimental data. Durotaxis [quantified as in (C)] represented as a function of the initial stiffness of the center of the cluster. For steep (red, 57 kPa/mm) and shallow (blue, 14 kPa/mm) gradients, horizontal bars indicate the mean values of the soft and the stiff edge at $t = 0$ hours. For uniform stiffness gels (orange), horizontal bars represent the stiffness SD of the gels in the group. Error bars are SD of $n = 3$ to 9 clusters. (E and F) Example of a control cluster (E) and a blebbistatin-treated cluster (F) expanding on a gradient gel. (G and H) Angle distribution of cell trajectories for control experiments (G) and blebbistatin (H). (I and J) An expanding cluster on a gradient gel before (I) and after (J) being severed by two laser cuts parallel to the midline applied at $t \sim 260$ min (white arrows). (K and L) Angular distributions of cell trajectories before (K) (140 to 230 min) and after (L) (400 to 490 min) laser ablation. See also fig. S12 and movie S10.

REFERENCES AND NOTES

1. R. Majumdar, M. Sixt, C. A. Parent, *Curr. Opin. Cell Biol.* **30**, 33–40 (2014).
2. P. Roca-Cusachs, R. Sunyer, X. Trepat, *Curr. Opin. Cell Biol.* **25**, 543–549 (2013).
3. C.-M. Lo, H.-B. Wang, M. Dembo, Y. L. Wang, *Biophys. J.* **79**, 144–152 (2000).
4. B. C. Isenberg, P. A. Dimilla, M. Walker, S. Kim, J. Y. Wong, *Biophys. J.* **97**, 1313–1322 (2009).
5. M. Raab et al., *J. Cell Biol.* **199**, 669–683 (2012).
6. S. V. Plotnikov, A. M. Pasapera, B. Sabass, C. M. Waterman, *Cell* **151**, 1513–1527 (2012).
7. T. Kawano, S. Kidoaki, *Biomaterials* **32**, 2725–2733 (2011).
8. J. R. Tse, A. J. Engler, *PLOS ONE* **6**, e15978 (2011).
9. L. G. Vincent, Y. S. Choi, B. Alonso-Latorre, J. C. del Álamo, A. J. Engler, *Biotechnol. J.* **8**, 472–484 (2013).
10. L. Bollmann et al., *Front. Cell. Neurosci.* **9**, 363 (2015).
11. L. A. Flanagan, Y.-E. Ju, B. Marg, M. Osterfield, P. A. Janmey, *Neuroreport* **13**, 2411–2415 (2002).
12. F. Liu et al., *J. Cell Biol.* **190**, 693–706 (2010).
13. T. A. Ulrich, E. M. de Juan Pardo, S. Kumar, *Cancer Res.* **69**, 4167–4174 (2009).
14. D. Cai et al., *Cell* **157**, 1146–1159 (2014).
15. E. Donà et al., *Nature* **503**, 285–289 (2013).
16. A. Haeger, K. Wolf, M. M. Zegers, P. Friedl, *Trends Cell Biol.* **25**, 556–566 (2015).
17. A. Bianco et al., *Nature* **448**, 362–365 (2007).
18. B. A. Camley, J. Zimmermann, H. Levine, W.-J. Rappel, *Phys. Rev. Lett.* **116**, 098101 (2016).
19. G. Malet-Engra et al., *Curr. Biol.* **25**, 242–250 (2015).
20. E. Thevenneau et al., *Dev. Cell* **19**, 39–53 (2010).
21. R. Sunyer, A. J. Jin, R. Nossal, D. L. Sackett, *PLOS ONE* **7**, e46107 (2012).
22. Materials and methods are available as supplementary materials on Science Online.
23. A. Elosegui-Artola et al., *Nat. Mater.* **13**, 631–637 (2014).
24. D. T. Tambe et al., *Nat. Mater.* **10**, 469–475 (2011).
25. E. Bazellieres et al., *Nat. Cell Biol.* **17**, 409–420 (2015).
26. C. E. Chan, D. J. Odde, *Science* **322**, 1687–1691 (2008).
27. A. Elosegui-Artola et al., *Nat. Cell Biol.* **18**, 540–548 (2016).
28. J. Escribano, M. T. Sánchez, J. M. García-Aznar, *Comput. Part. Mech.* **1**, 117–130 (2014).
29. A. Berdahl, C. J. Torney, C. C. Ioannou, J. J. Faria, I. D. Couzin, *Science* **339**, 574–576 (2013).
30. P. M. Krafft, R. X. Hawkins, A. S. Pentland, N. D. Goodman, J. B. Tenenbaum, in *Proceedings of the 37th Conference of the Cognitive Science Society* (Cognitive Science Society, 2015).

ACKNOWLEDGMENTS

The authors acknowledge X. Serra-Picamal, V. Romaric, R. Alert, J. Cadademunt, and all members of the X.T. and P.R.-C. laboratories for stimulating discussions; N. Castro for technical assistance; and G. Charras, G. Scita, and E. Sahai for providing cells. This work was supported by the Spanish Ministry of Economy and Competitiveness (BFU2015-65074-P to X.T., BFU2011-23111 and BFU2014-52586-REDT to P.R.-C., DPI2015-64221-C2-1-R to J.M.G.-A., DPI2013-43727-R to J.J.M., PI14/00280 to D.N., RYC-2014-15559 to V.C., FPI BES-2013-063684 to J.E., IJCI-2014-19156 to A.E.-A., and IJCI-2014-19843 to A.L.), the Generalitat de Catalunya (2014-SGR-927), the European Research Council (CoG-616480 to X.T. and StG 306571 to J.M.G.-A.), Obra Social “La Caixa,” Marie-Curie Action (CAFFORCE 328664 to A.L.), EMBO Long-Term Fellowship (EMBO ALTF 1235-2012 to A.L.), a Career Integration Grant within the seventh European Community Framework Programme (PCIG10-GA-2011-303848 to P.R.-C.), and Fundació la Marató de TV3 (project 20133330 to P.R.-C.).

SUPPLEMENTARY MATERIALS

www.sciencemag.org/content/353/6304/1157/suppl/DC1
Materials and Methods
Supplementary Text
Figs. S1 to S16
Tables S1 and S2
Movies S1 to S10
References (31–43)

22 March 2016; accepted 27 July 2016
10.1126/science.aaf7119

TUMOR METABOLISM

Tissue of origin dictates branched-chain amino acid metabolism in mutant *Kras*-driven cancers

Jared R. Mayers,^{1,2*} Margaret E. Torrence,^{1,2*} Laura V. Danai,¹ Thales Papagiannakopoulos,^{1†} Shawn M. Davidson,^{1,2} Matthew R. Bauer,¹ Allison N. Lau,¹ Brian W. Ji,³ Purushottam D. Dixit,³ Aaron M. Hosios,^{1,2} Alexander Muir,¹ Christopher R. Chin,¹ Elizaveta Freinkman,^{1,2,4,5,6} Tyler Jacks,^{1,2,6} Brian M. Wolpin,⁷ Dennis Vitkup,³ Matthew G. Vander Heiden^{1,2,5,7‡}

Tumor genetics guides patient selection for many new therapies, and cell culture studies have demonstrated that specific mutations can promote metabolic phenotypes. However, whether tissue context defines cancer dependence on specific metabolic pathways is unknown. *Kras* activation and *Trp53* deletion in the pancreas or the lung result in pancreatic ductal adenocarcinoma (PDAC) or non-small cell lung carcinoma (NSCLC), respectively, but despite the same initiating events, these tumors use branched-chain amino acids (BCAAs) differently. NSCLC tumors incorporate free BCAAs into tissue protein and use BCAAs as a nitrogen source, whereas PDAC tumors have decreased BCAA uptake. These differences are reflected in expression levels of BCAA catabolic enzymes in both mice and humans. Loss of *Bcat1* and *Bcat2*, the enzymes responsible for BCAA use, impairs NSCLC tumor formation, but these enzymes are not required for PDAC tumor formation, arguing that tissue of origin is an important determinant of how cancers satisfy their metabolic requirements.

The development of new cancer therapeutics relies on underlying genetic features to identify sensitive patients (1). Mutations in both *KRAS* and *TP53* are common genetic events found in tumors arising from many tissues, and cancers with these mutations are often difficult to treat (2, 3). These genetic events, as well as others associated with cancer, contribute to the metabolic changes that support biomass accumulation and cancer cell proliferation (4). Oncogenic *RAS* signaling increases glucose and glutamine consumption to support anabolic processes including nucleotide, lipid, and nonessential amino acid biosynthesis and can also drive extracellular protein and lipid scavenging (5). *TP53* mutations increase glucose consumption and glycolytic flux, whereas inactivation of *TP53* renders cancer cells more dependent on serine uptake and metabolism (6).

KRAS and *TP53* mutations are found in most human pancreatic tumors (7) and are also common in lung adenocarcinoma (8). What is known of how mutant *KRAS* or disruption of *TP53* affects

cancer metabolism is based on cell culture studies in defined medium, although in vivo nutrient availability varies widely between tissues, and vasculature changes can limit nutrient access within tumors (9, 10). The inability to model these differences in culture has therefore limited understanding of how tissue of origin influences tumor metabolism (11). Furthermore, environment can influence metabolic phenotypes in vitro (12–14), and metabolic dependencies in vivo can differ from those found in vitro (15). Metabolic differences between tumor types may also result from cell-autonomous effects, and tumor metabolic gene expression more closely resembles that of its tissue of origin than that of other tumors (16). The same oncogenic driver can also cause different metabolic phenotypes in lung and liver tumors (17). This raises the possibility that tumor type is a major determinant of some tumor metabolic dependencies in vivo.

Elevated plasma branched-chain amino acid (BCAA) levels are found in early pancreatic ductal adenocarcinoma (PDAC) but not in non-small cell lung carcinoma (NSCLC), even when the tumors are initiated by the same genetic events (18). To confirm that tumor tissue of origin influences whole-body BCAA metabolism, we used *LSL-Kras^{G12D/+};Trp53^{fllox/fllox}* (KP) mice. We crossed KP mice to mice harboring a *Cre-recombinase* allele driven by a *Pdx-1* promoter (KP^{-/-C} model) (19) or delivered viral *Cre* to the lungs of these mice (20) in order to generate models of PDAC and NSCLC, respectively. Consistent with prior reports (18), mice with early PDAC have increased levels of plasma BCAAs, whereas mice with early NSCLC exhibit decreased plasma BCAA levels (fig. S1, A to D). When cells derived from these tumors

¹Koch Institute for Integrative Cancer Research, Massachusetts Institute of Technology, Cambridge, MA 02139, USA. ²Department of Biology, Massachusetts Institute of Technology, Cambridge, MA 02139, USA. ³Center for Computational Biology and Bioinformatics and Department of Systems Biology, Columbia University, New York, NY 10027, USA. ⁴Whitehead Institute for Biomedical Research, Nine Cambridge Center, Cambridge, MA 02142, USA. ⁵Broad Institute, Seven Cambridge Center, Cambridge, MA 02142, USA. ⁶Howard Hughes Medical Institute, Massachusetts Institute of Technology, Cambridge, MA 02139, USA. ⁷Dana-Farber Cancer Institute, Boston, MA 02115, USA.

*These authors contributed equally to this work.

†Present address: School of Medicine, New York University, New York, NY 10016, USA. ‡Corresponding author. Email: mvh@mit.edu

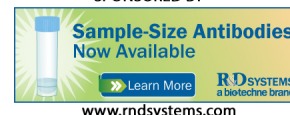


Collective cell durotaxis emerges from long-range intercellular force transmission

Raimon Sunyer, Vito Conte, Jorge Escribano, Alberto Elosegui-Artola, Anna Labernadie, Léo Valon, Daniel Navajas, José Manuel García-Aznar, José J. Muñoz, Pere Roca-Cusachs and Xavier Trepát (September 8, 2016)
Science **353** (6304), 1157-1161. [doi: 10.1126/science.aaf7119]

Editor's Summary

EXTENDED PDF FORMAT
SPONSORED BY



This copy is for your personal, non-commercial use only.

- | | |
|----------------------|--|
| Article Tools | Visit the online version of this article to access the personalization and article tools:
http://science.sciencemag.org/content/353/6304/1157 |
| Permissions | Obtain information about reproducing this article:
http://www.sciencemag.org/about/permissions.dtl |

Science (print ISSN 0036-8075; online ISSN 1095-9203) is published weekly, except the last week in December, by the American Association for the Advancement of Science, 1200 New York Avenue NW, Washington, DC 20005. Copyright 2016 by the American Association for the Advancement of Science; all rights reserved. The title *Science* is a registered trademark of AAAS.